ACS OMEGA

Open Access

http://pubs.acs.org/journal/acsodf

Article

Controllable Preparation and Thermochemical Properties of Ultrafine FOX-7 by Microfluidic Crystallization Strategy

Hanyu Jiang, Xuanjun Wang,* Siyu Xu, Jin Yu, Zihao Zhang, Xiaogang Mu, Taizhong Huang, and Fengqi Zhao

Cite This: *ACS Omega* 2025, 10, 14042−14051

Read Online

ACCESS | Metrics & More | Article Recommendations

ABSTRACT: The 1,1-diamino-2,2-dinitroethylene (FOX-7) has been adopted in high-energy explosives. To further improve the thermal safety and detonation performance of FOX-7, a microfluidic crystallization platform with a swirl-shaped chip was employed to prepare ultrafine FOX-7. Results show that the crystal structure of FOX-7 could be precisely controlled by adjusting the operational parameters of microfluidic. The microfluidic techniques prepared superfine FOX-7 exhibit a consistent smaller particle size, narrower particle size distribution, reduced crystal defects, and enhanced sphericity structure. On the other hand, the thermochemical properties of FOX-7 are also improved. The thermal decomposition temperature and critical thermal explosion temperature of ultrafine FOX-7 are increased by 24.6 and 22.1 °C, respectively. The thermal stability, energy release efficiency, and combustion of the microfluidic recrystallization method prepared FOX-7 are greatly improved. This research presents a secure, effective, and eco-friendly methodology for the preparation and manipulation of ultrafine FOX-7 crystals.

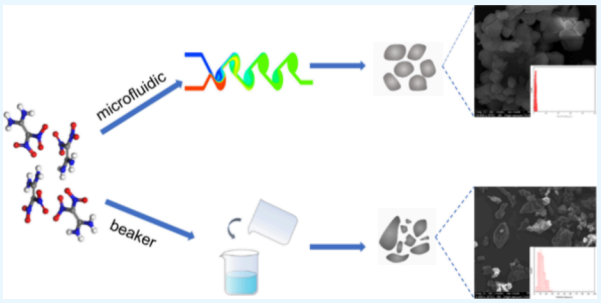

1. INTRODUCTION

1,1-Diamino-2,2-dinitroethylene (FOX-7) is a promising insensitive explosive with excellent comprehensive properties, which was first synthesized in 1998 and has attracted great attention from energetic materials researchers.[1−4] However, no matter what kind of synthesis process is adopted, FOX-7 products exhibit certain limitations such as inadequate densification, uneven particle size distribution, and irregular crystal morphology, which eventually limit their applications.[5−8] Recrystallization, as one of the most practical methods to prepare super-refinements and to improve the performance of explosives, plays a crucial role in crystal shape and morphology improvement. Currently, batch kettle crystallization is widely applied in crystallization processes despite the drawbacks of inconsistent product quality and high operational costs. How to improve the quality of FOX-7 has been investigated by many scientists.

In all of the developed methods, continuous microfluidic crystallization exhibits great promise.[9−12] Microfluidic technology, which enables rapid and homogeneous blending of different fluids at a microscale within microtubules or microchips,[13] emerged during the 1990s[14] and has been applied in diverse fields, such as the preparation of fine chemicals,[15,16] synthesis of drugs, etc.[17−19] Microfluidics have significant spatial effects due to their large specific surface area, which can effectively increase the mass and heat transfer of fluid. Compared with the conventional crystallization method, microfluidic crystallization technology has the advantages of precise controlling crystallization environment, minimal online sample volume, high throughput screening capabilities, and low operational costs.[20,21] Microfluidic crystallization technology can overcome the shortage of transitional technology, such as inconsistent quality of existing explosives and poor batch stability. This technology is especially suitable for the continuous preparation of energetic materials with ultrafine morphology.[22−26]

To the best of our knowledge, there have been no reports about the preparation of micronano FOX-7 using the microfluidic crystallization method. In this paper, a microfluidic crystallization strategy for the preparation of ultrafine FOX-7 was proposed and a comparison in crystal morphology between the traditional batch method and microfluidic method was made. Furthermore, the thermal properties and laser ignition combustion performance of FOX-7 samples prepared by using microfluidic crystallization were investigated, which further substantiated the potential of microfluidic technology in refining energetic materials.

Received: December 5, 2024
Revised: January 12, 2025
Accepted: January 21, 2025
Published: April 7, 2025

2. EXPERIMENTAL SECTION

2.1. Regents and Materials. FOX-7 with a mass fraction purity of 98% was synthesized by Xi'an Modern Chemistry Research Institute (Xi'an, China). Dimethyl sulfoxide (DMSO), *N*,*N*-dimethylformanmide (DMF), and anhydrous ethanol were of analysis reagent grade and purchased from Aladdin Biochemical Technology Co., Ltd. (Shanghai, China). For the experiments, the deionized water was obtained through double purification using a sub-boiling distillation device.

2.2. Microfluidic Simulation. The two-phase fluid mixing in microfluidic chips was investigated using ANSYS FLUENT software. The inlet fluids are water and DMSO respectively and are set as viscous and incompressible fluids. The physical property parameters of H_2O and DMSO are shown in Table 1. The mesh is divided into hexahedral elements.

Table 1. Physical Property Parameters of Two-Phase Fluids

reaction fluid	density (kg m^{-3})	viscocity (kg m^{-1} s^{-1})	mass diffusivity (m^2 s^{-1})
H_2O	998.2	0.001003	1.2×10^{-9}
DMSO	1100	0.001987	1.2×10^{-9}

The mixing performance of the microfluidic chip was further investigated by calculating a mixing index M, ranging from 0 to 1, using eq 1.[27,28]

$$M = 1 - \sqrt{\frac{1}{N}\sum_{1}^{N}\left(\frac{C_i - C_{\text{mix}}}{C_{\text{unmix}} - C_{\text{mix}}}\right)^2} \quad (1)$$

where C_i represents the concentration or mass fraction of one unit in the selected area, C_{unmix} and C_{mix} represent the concentration or mass fraction before and after completely mixing, respectively, and N represents the number of duplicate units. By utilization of the equation mentioned above, it can be observed that when M equals 0, there is no mixing between the two fluids at all. Conversely, when M equals 1, complete mixing occurs between them.

2.3. Preparation of Ultrafine FOX-7. The microfluidic crystallization platform for the production of ultrafine FOX-7 is depicted in Figure1, comprising a pair of infusion pumps, a microfluidic chip, a collection device, and interconnected Teflon tubes. The microfluidic chip is a six-chamber swirl-shaped structure; both the inlet and outlet width are 1 mm, the channel diameter is 5 mm, the depth is 500 μm, and the inner diameter and outer diameter of the Teflon tube are 1 mm and 2 mm, respectively. The solvent and antisolvent were propelled through the tube at varying flow rates by using infusion pumps. Following the swirling motion within the micromixer, a yellow colloidal liquid passed through the tube, and ultrafine FOX-7 particles were obtained via filtration and freeze-drying procedures. The entire process of recrystallization was conducted at room temperature (25 °C)

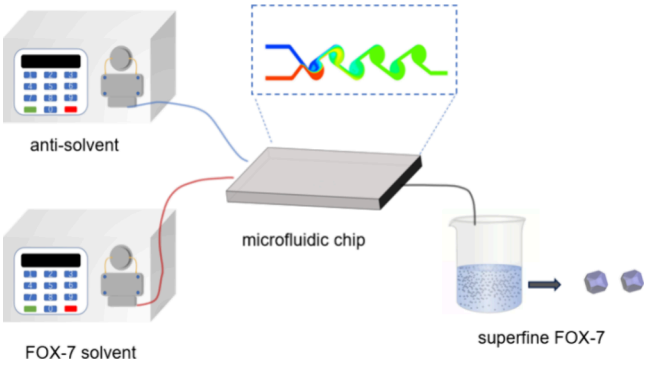

Figure 1. Schematic diagram of the microfluidic platform.

To demonstrate the superiority of the micromixer in the preparation of ultrafine FOX-7, a control sample was also prepared using a beaker under identical experimental parameters in this study, as illustrated in Figure 2.

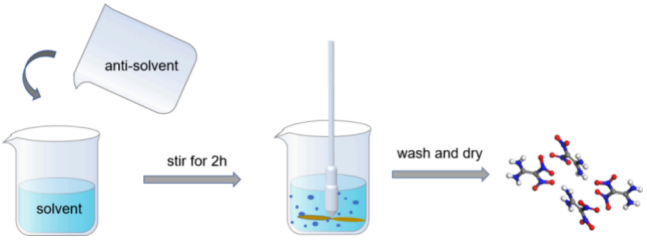

Figure 2. Preparation process of ultrafine FOX-7 by beaker.

2.4. Characterization Methods. The structure and crystal phase were investigated by using X-ray diffraction (XRD) with a PANalytical Empyrean diffractometer equipped with a Cu Kα source and working at 40 kV and 40 mA. The XRD data was collected within the range of 5 to 70° (2θ) with an increment of 0.02°. Scanning electron microscopy (SEM) test was employed to investigate the morphology using FEI JSM-5800 (Hitachi, Japan). The particle size distributions (PSD) of the samples were analyzed by Nanomeasure software on a sample set of 200 particles.

The differential scanning calorimetry tests were conducted by using a DSC 204 HP (NETZSCH, Germany) in a nitrogen atmosphere with a flow rate of 50 mL·min^{-1}, and the temperature ranges were set from ambient temperature to 350 °C. The sample mass for the DSC test was about 1 mg. The heating rates were set as 5, 10, 15, and 20 K·min^{-1}.

The laser ignition and combustion tests were conducted by using a CO_2 continuous laser (SLC 110, Coherent, USA) with a maximum power output of 120 W with a wavelength of 10.6 μm. The laser spot diameter is 5.0 mm. The flame images during the combustion processes were captured by using a high-speed digital camera with an operating rate of 1000 frames per second. To minimize the experimental errors, each test was repeated three times and the average value was adopted to analyze the ignition characteristics of the materials.

3. RESULTS AND DISCUSSION

3.1. Simulation and Optimization of Microfluidic in Different Chips. The microfluidic chip serves as the core component of the microfluidic crystallization system, and its internal microchannel structure exerts a profound influence on both crystal nucleation and growth processes.[29] Based on the presence or absence of an external power source, it can be categorized into active hybrid type and passive hybrid type. Both heart-shaped and swirl-shaped chips belong to the passive hybrid category, wherein they primarily manipulate fluid velocity and direction through specialized microchannel structures. These structures effectively induce repeated division, stretching, twisting, or folding of initially parallel streamlines to enhance convective diffusion and facilitate rapid mixing. The flow distribution, velocity contour diagrams, and

https://doi.org/10.1021/acsomega.4c10924
ACS Omega 2025, 10, 14042−14051

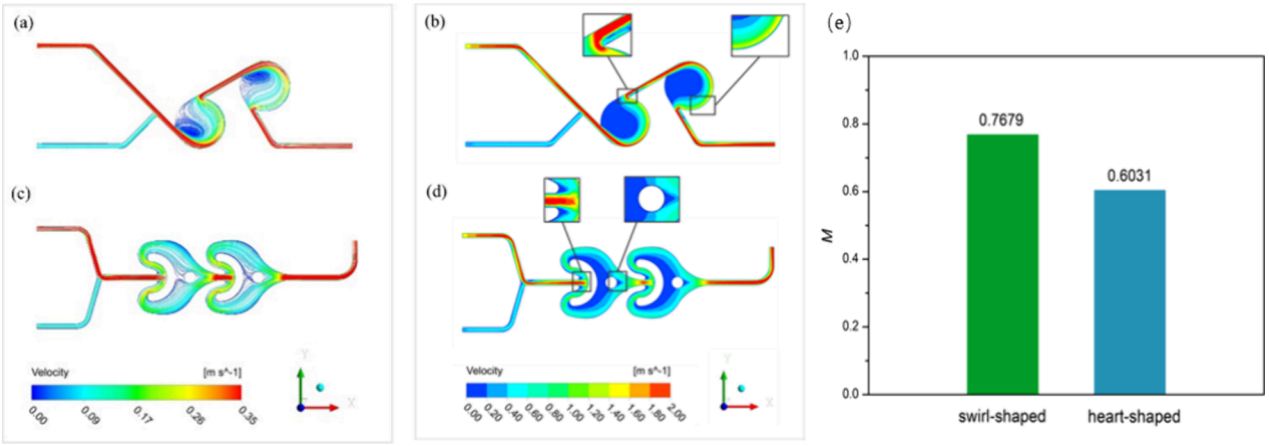

Figure 3. Modulated flow distribution and velocity contour diagram of (a, b) heart-shaped and (c, d) swirl-shaped chips. (e) Mixing index of two microfluidic chips.

mixing index (M) of heart-shaped and swirl-shaped chips are shown in Figure 3 with a flow ratio R of 5.

Figure 3 shows that to the heart-shaped chip, the fluid velocity is significantly accelerated after passing through the narrow channel. The strong inertial force causes the fluid with higher flow velocity to spread along the wall toward the entire chamber. However, the utilization of the central region is rather low, which results in the formation of a "dead zone" of velocity. On the other hand, to the swirl-shaped chip, a distinct vortex is formed near the entrance of the chamber, which gradually intensifies linearly before moving away from the wall due to external flow. Upon reaching a certain extent, the occurrence of instability and fragmentation leads to turbulence that enhances the convection among different components within the fluid field. This turbulence disrupts the boundary layers, reduces concentration polarization, and promotes mass transfer processes. These findings demonstrate that, compared to heart-shaped chips, the swirl-shaped chip not only exhibits superior mixing effects but also experiences lower shear forces, which reduces the crystal collisions and inhibits secondary nucleation. It is also ever reported that the swirl-shaped chip is more suitable for practical applications involving brittle crystal preparation.[30]

Figure 4 shows the correlation of the mixing index of the swirl chip with the number of chambers under different flow rates. The two-phase liquid flow ratio R is 1, and the total flow rates are 10, 20, and 50 mL min^{-1}, respectively. Figure 4 distinctly reveals that the mixing index changes in similar rules under the three flow conditions. With the increase of chamber number, the mixing index gradually increases and tends to be stabilized when the number surpasses 4. It also reveals that the mixing indices corresponding to the three flow conditions are 0.9583, 0.9612, and 0.9604. Therefore, a six-chamber swirl-shaped chip is selected for sample preparation in this study.

3.2. Comparison between the Beaker Method and Microfluidic Method. The particle size and morphology of the recrystallized explosive are greatly influenced by the mixing efficiency and uniformity. The recrystallization process of FOX-7 is fairly fast. The particles of FOX-7 with uniform crystal morphology and narrow size distribution can be obtained only under the condition of high mixing uniformity of micronano crystals. To investigate the microscale effect of microfluidic crystallization, DMSO and ethanol were used as the solvent and antisolvent. FOX-7 dissolved in DMSO with a

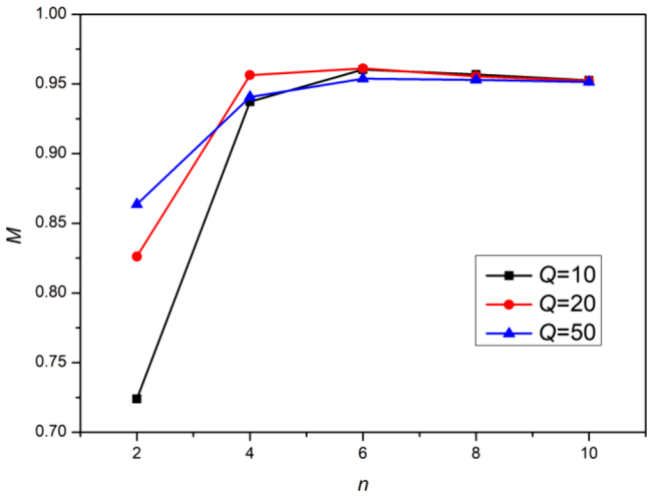

Figure 4. Mixing index curve of the swirl-shaped chip under different flow conditions.

fixed concentration of 0.15g·mL^{-1} is mixed with antisolvent with a fixed flow ratio of 5. For the micromixer preparation, the total flow rate was set at 25 mL·min^{-1}. Ultrafine FOX-7 prepared by both the traditional beaker method and the microfluidic method were compared. The crystal morphology and particle size distribution of the obtained materials are shown in Figure 5.

The comparison of Figure 5a–c shows that recrystallized FOX-7 exhibits a smaller average particle size and a narrower particle size distribution compared to the raw material. FOX-7 prepared by using the beaker method displays an irregular shape with small particles adhering to larger ones. The average particle size is 10.47 μm with the distribution range from 5.35 to 19.09 μm. However, FOX-7 prepared by the microfluidic method exhibits greater regularity, smoother surfaces without noticeable edges or defects, and improved sphericity that could be attributed to efficient mass and heat transfer during the preparation process. The particle sizes range from 0.95 to 3.78 μm, with an average size of 2.41 μm. It is clearly proved that the FOX-7 prepared on this platform possesses smaller particle sizes, narrower PSDs, and fewer crystal defects than those prepared in beakers. To further investigate the structure of FOX-7 that was prepared by different methods, the X-ray

https://doi.org/10.1021/acsomega.4c10924
ACS Omega 2025, 10, 14042−14051

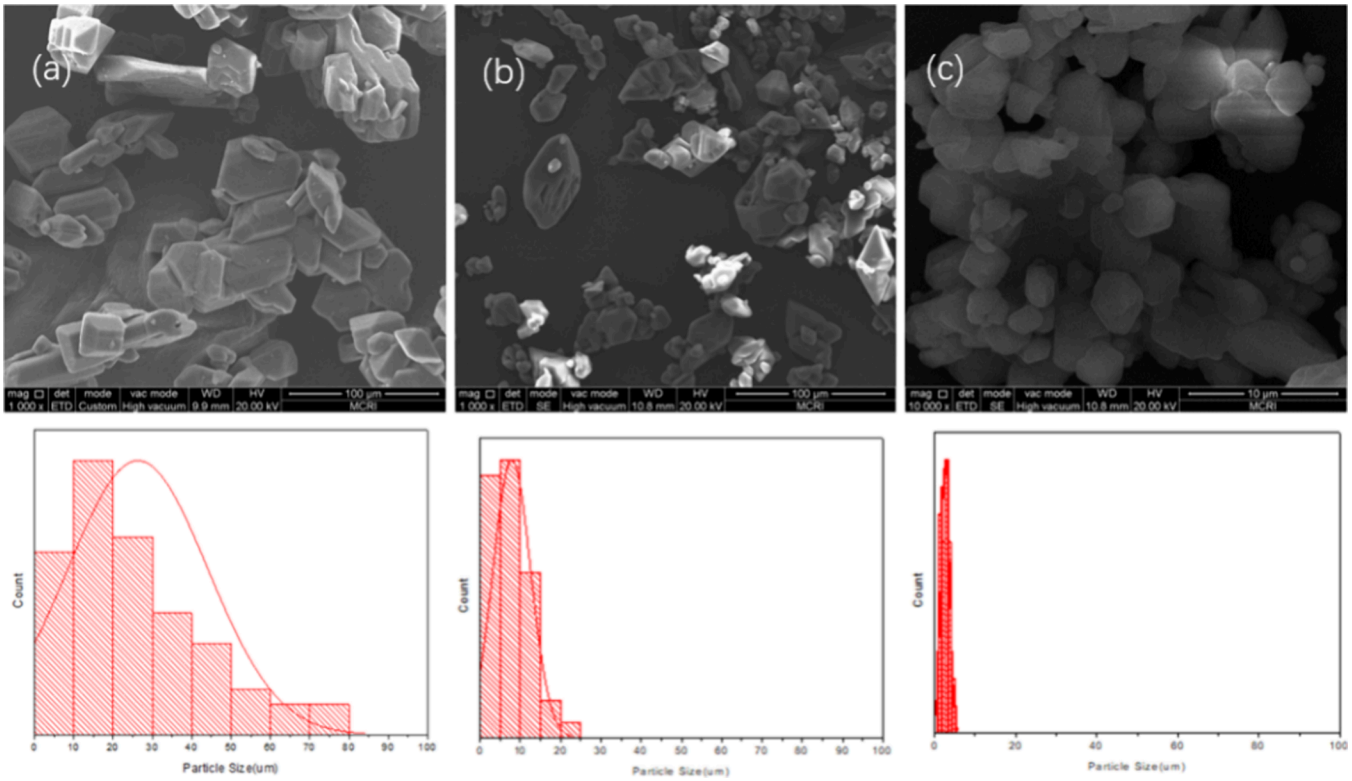

Figure 5. SEM images and PSDs of FOX-7 prepared by different methods. (a) Raw; (b) prepared by the beaker method; (c) prepared by the microfluidic method.

diffraction tests were conducted, and the obtained results are shown in Figure 6.

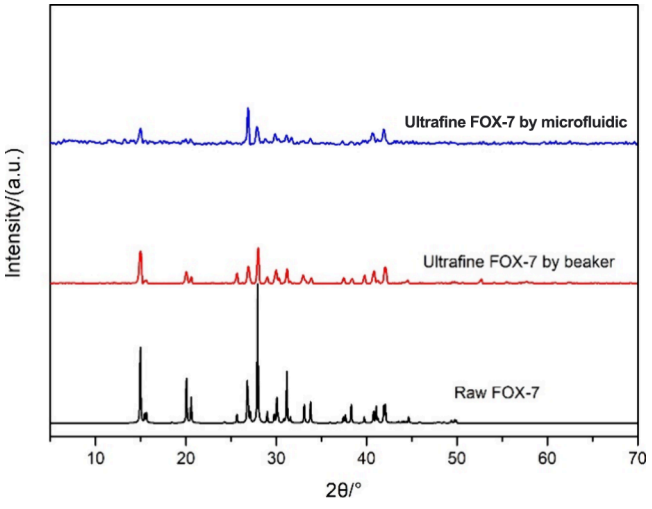

Figure 6. XRD patterns of samples prepared by different methods.

The XRD test results in Figure 6 distinctly show the FOX-7 particles prepared using both the microfluidic platform and the beaker. The diffraction pattern of the raw material FOX-7 reveals four prominent peaks at the 2θ diffraction peaks of 27.9, 26.8, 20.6, and 15.0°, which correspond to (0 2 1), (0 2 0), (1 1 1), and (1 0 1), respectively, which proved the existence of α-FOX-7. The diffraction peaks of ultrafine FOX-7 prepared by using different methods are consistent with each other, which means that the crystal structure of α-FOX-7 remained constant despite different preparation methods. In addition, compared to the raw material, certain crystal faces of ultrafine FOX-7 display reduced intensity and broader width in their X-ray diffraction spectra due to pronounced micronano effects observed consistently with SEM results.

3.3. Crystal Morphology and Particle Size Control of Ultrafine FOX-7 Prepared by the Microfluidic Method.

3.3.1. Effect of the Solvents on Crystal Morphology. Crystal morphology prediction studies have demonstrated the significant influence of the solvent/antisolvent system on crystal growth.[31] Microfluidics, in comparison to conventional methods, offers a superior crystallization environment that is more suited for validating predicted outcomes and achieving precisely controlled explosive morphologies. In order to explore the effect of solvent on FOX-7 crystal morphology, DMSO and DMF were utilized as solvents, while anhydrous ethanol and deionized water were employed as antisolvents with a constant solvent/antisolvent flow ratio of 5. The experiments were conducted on a well-established microfluidic platform. The morphology of FOX-7 obtained from different solvent systems was examined by SEM tests, and the obtained results are shown in Figure 7.

It is evident from the figures that the crystal structure changes greatly with different solvent systems. The crystal sphericity of the FOX-7 obtained from the solvent of DMSO/EtOH and DMF/EtOH systems is obviously better than that of DMSO/H_2O and DMF/H_2O systems. This phenomenon can be ascribed to the adsorption of solvent and antisolvent molecules onto the surface of FOX-7 crystals through hydrogen bonding and other intermolecular forces, which results in a solvation effect that significantly alters the relative growth rate and crystallization at different crystal facets. When water is employed as the antisolvent, the FOX-7 crystal exhibits significant stacking growth, characterized by an

https://doi.org/10.1021/acsomega.4c10924
ACS Omega 2025, 10, 14042−14051

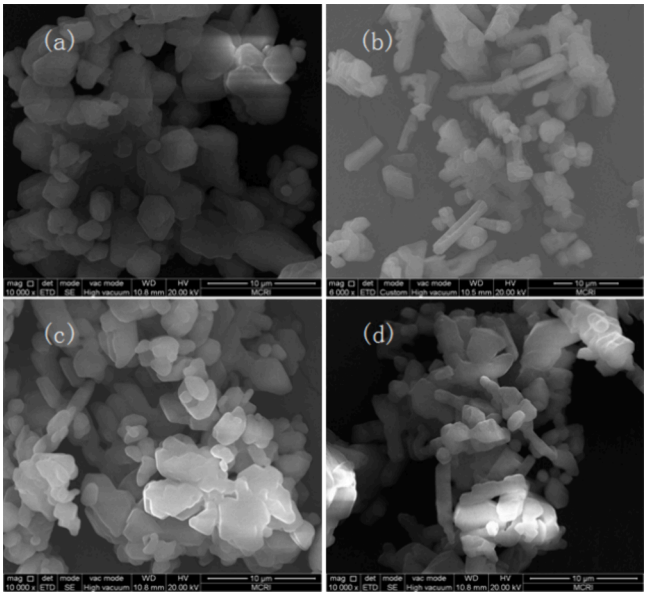

Figure 7. Morphologies of FOX-7 prepared by different solvent/antisolvent systems. (a) DMSO/EtOH; (b) DMSO/H_2O; (c) DMF/EtOH; (d) DMF/H_2O.

elongated rod-like morphology and uneven particle size distribution. Conversely, substituting ethanol as the antisolvent results in regularity in crystal growth with excellent dispersion and a uniform particle size distribution. The crystal that grows under DMSO shows a spheroidal shape with excellent particle dispersion and uniform size distribution, while that obtained from DMF appears massive and exhibits particle agglomeration. Additionally, the solubility of FOX-7 in DMSO surpasses that in DMF[32], which means less solvent consumption in the preparation process. The aforementioned experimental results demonstrate that the DMSO/EtOH solvent system exhibits superior efficacy in the synthesis of ultrafine FOX-7, thereby warranting its selection for subsequent investigations.

3.3.2. Effect of the Concentration on Particle Size. To investigate the influence of concentration on the crystallization of FOX-7 that was prepared by the microfluidic method, ultrafine particles were prepared by dissolving varying quantities of FOX-7 were prepared using DMSO/ethanol as solvent/antisolvent system with a fixed value of 3. The concentrations of FOX-7 were set as 0.075, 0.15, and 0.2 g·mL^{-1}. Figures 8 and 9 show the morphology and PSDs of ultrafine FOX-7 obtained at different concentrations. Figure 7 clearly shows that the crystal morphology of all of the FOX-7 obtained at the three concentrations is spherical with different particle sizes and distributions. For a concentration of 0.075 g·mL^{-1}, the size of the prepared FOX-7 particles exhibits a size distribution ranging from 5.58 to 13.76 um. At a concentration of 0.15 g·mL^{-1}, the particle size range narrows down to 2.43−6.35 um, whereas at a higher concentration of 0.2 g·mL^{-1}, it further decreases to the range of 0.95−4.28 um. Figure 8 also shows that the particle size distribution becomes narrower with the increase of FOX-7 concentration in the microfluidic system of DMSO/ethanol. On the other hand, the average particle size also has a slight decrease at the same time. The variation in particle size can be readily explained from a supersaturation perspective. According to the crystallization dynamics theory in the liquid phase, both nucleation rate (R_N) and growth rate (R_G) can be mathematically described using the Arrhenius formula (eq 2):[33]

$$\begin{cases} R_N = \dfrac{dN}{dt} = k_n S^n \\ R_G = \dfrac{dN'}{dt} = k_g S^g \end{cases} \quad (2)$$

where the rate constants of nucleation and growth are denoted as k_n and k_g, respectively. The exponential values of growth rate and nucleation rate are represented by n and g, while supersaturation is indicated by S. Generally, the value of k_g ranges from 1 to 2, whereas the value of k_n falls between 5 and 10.[34] As the flow ratio increases, supersaturation also increases, which leads to the nucleation rate becoming the rate-determining step in crystallization and results in a decrease in particle size. Consequently, by adjusting the concentration of FOX-7 in DMSO, it is possible to regulate the crystal size.

3.3.3. Effect of the Flow Rate on Particle Size. The antisolvent and solvent have different surface active energies, which can greatly influence the recrystallization of FOX-7. In this paper, the flow ratio of DMSO/ethanol on the recrystallization of FOX-7 was investigated. The solvent injection volume flow rate was fixed at 5 mL·mL^{-1}, with the FOX-7 concentration of 0.2 g·mL^{-1}. The antisolvent/solvent flow ratio (R) values were set as 1, 3, 5, 10, and 15. The PSD and particle sizes of the obtained FOX-7 are illustrated in Figure 10. Figure 10 shows that for R = 1, the particle size of FOX-7 ranges from 1.73 to 5.26 μm. For R = 3, it ranges from 1.34 to 4.28 μm. For R = 5, it ranges from 0.95 to 2.63 μm. For R = 10, it ranges from 0.94 to 2.12 μm. For R = 15, it ranges from 0.77 to 1.66 μm. Furthermore, the average particle size (D_{50}) of FOX-7 prepared with R values of 1, 3, 5, 10, and 15 are 2.74, 2.44, 1.79, 1.54, and 1.21 μm, respectively. It is evident that the increased R leads to a gradual reduction of the particle size of ultrafine FOX-7. Figure 10 also shows that the PSD is narrowed with the increase in flow ratio. On the other hand, Figure10 also shows that with the increase of R, the PSDs exhibit gradual changes. The rapid increase in supersaturation with increasing antisolvent concentration leads to the nucleation rate becoming the rate-determining step, which promotes the formation of crystals with smaller particle sizes. Additionally, the increase of flow ratio R also improves the mixing efficiency, and the rapid mixing and frequent collision between solvent and antisolvent at the microscale reduce the concentration gradient in the system and eventually reduce the PSD and make the particle size more uniform.

The above results reveal that the crystal morphology in the microfluidic platform can be precisely modulated by fine-tuning the solvent/antisolvent system, while the particle size and PSD can be effectively regulated through the adjustment in concentration and flow ratio.

3.4. Thermal Behavior and Thermal Safety. The thermal analysis data for raw FOX-7 and ultrafine FOX-7 samples are presented in Figure 11 and Table 2, respectively. The thermal behavior of the prepared ultrafine FOX-7 during its thermal decomposition process exhibits similarities to that of the pristine material FOX-7, which has undergone two processes of phase transformation and decomposition.[35,36] The phase transition process includes $\alpha \rightarrow \beta$ (the first crystal peak of 115−117 °C) and $\beta \rightarrow \gamma$ (the second crystal peak of 170−190 °C). The decomposition process also consists of two stages. The first stage corresponds to the initial exothermic

https://doi.org/10.1021/acsomega.4c10924
ACS Omega 2025, 10, 14042−14051

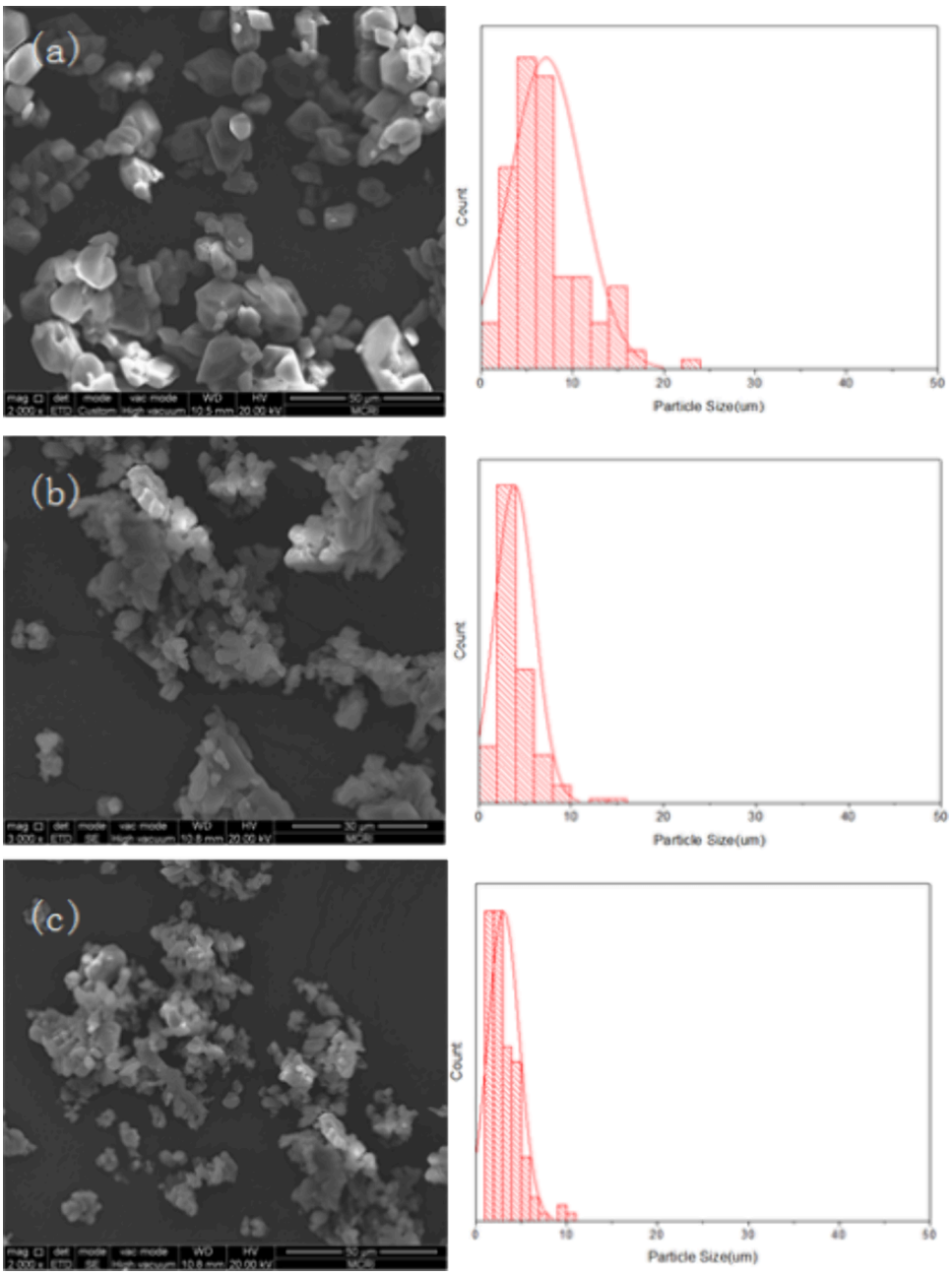

Figure 8. Morphologies and PSDs of Fox-7 samples prepared with different concentrations of (a) 0.075, (b) 0.15, and (c) 0.2 g·mL^{-1}.

decomposition, which takes place within the temperature range of 210−250 °C. This can be attributed to the rearrangement of the nitro group in FOX-7, resulting in the disruption of both the conjugated system and hydrogen bonds, ultimately leading to the cleavage of the nitro group and subsequent generation of nitric oxide. The second exothermic decomposition stage occurs within the temperature range of 260−300 °C and primarily arises from carbon skeleton fragmentation within FOX-7 molecules. In comparison with raw FOX-7, ultrafine FOX-7 exhibits a delayed second crystallization peak temperature by 11.5 °C and an increased initial exothermic peak temperature by 24.6 °C, phenomena that can be elucidated through "topological chemical reaction theory".[37−39] The decomposition temperatures of smaller FOX-7 particles generally tend to be higher due to their reduced lattice defects and lower internal stresses. In addition, compared with the raw material decomposition heat release temperature range (232.4−291.4 °C), the ultrafine FOX-7 decomposition heat release process concentrated in a narrower temperature range (257.0−270.6 °C), and the enthalpy of thermal decomposition increased from 1813 to 2145 J·g^{-1}. This means that the ultrafine FOX-7 prepared by microfluidic not only has good thermal stability but also has higher energy release efficiency.

The decomposition kinetics of FOX-7 samples were investigated, and the activation energy (E) and preexponential factor (A) of the initial decomposition process were determined using Kissinger's method (eq 3).[40,41]

$$\ln\left(\frac{\beta}{T_p}\right) = \ln\frac{AR}{E} - \frac{E}{R} \times \frac{1}{T_p} \tag{3}$$

https://doi.org/10.1021/acsomega.4c10924
ACS Omega 2025, 10, 14042−14051

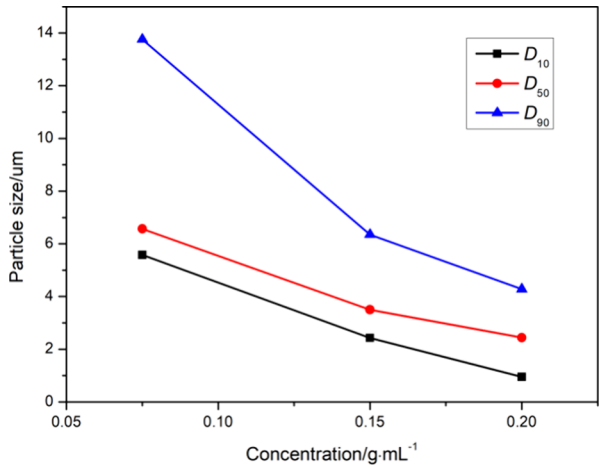

Figure 9. Influence of concentrations on particle size.

The parameter β represents the heating rate, while Tp denotes the peak temperature of the initial decomposition. The gas constant R is defined as 8.314 J·mol^{-1}·k^{-1}.

The critical thermal explosion temperature (T_b) plays a crucial role in the assessment of thermal safety for energetic materials. The T_b of raw and ultrafine FOX-7 obtained by microfluidic can be calculated by Zhang-Hu-Xie-Li's equation (eq 4).[42]

$$T_b = \frac{E - \sqrt{E^2 - 4ERT_{p0}}}{2R} \quad (4)$$

$$T_{pi} = T_{p0} + a\beta_i + b\beta_i^2 + c\beta_i^3, i = 1 \sim 4 \quad (5)$$

where the T_{p0} values corresponding to $\beta \rightarrow 0$ are computed from eq 5. a, b, and c represent coefficients. All kinetic parameters and thermal safety parameters are listed in Table 3. The E values for raw and ultrafine FOX-7 are 326.8 and 257.9 KJ·mol^{-1}, whereas the lg(A) values are 32.4 and 24.6, respectively. T_{p0} and T_b are 220.6 and 221.8 °C for raw Fox-7, while they are 242.1 and 243.9 °C for ultrafine Fox-7, respectively. The results indicate that FOX-7 prepared by microfluidic has better reactivity and higher thermal stability than the raw material. This is because the ultrafine FOX-7 has

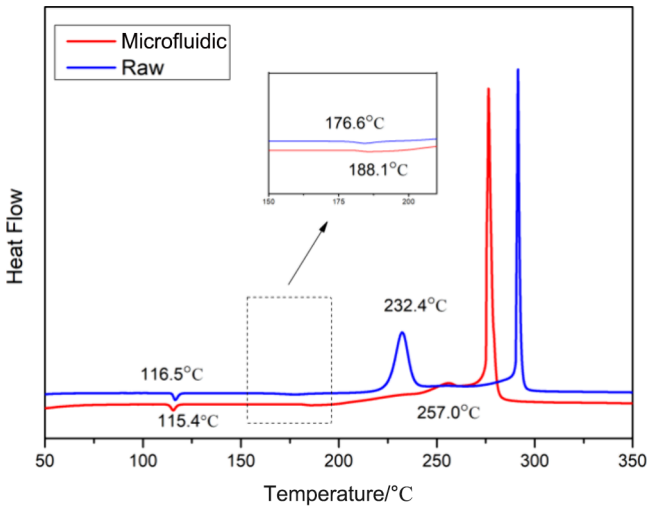

Figure 11. DSC curves of ultrafine and raw FOX-7.

Table 2. Thermal Analysis Parameters of Ultrafine and Raw Fox-7

	phase transition process		decomposition process		
samples	T_{p1}/°C	T_{p2}/°C	T_{p1}/°C	T_{p2}/°C	ΔH/J g^{-1}
raw Fox-7	116.5	176.6	232.4	291.4	1813
ultrafine Fox-7	115.4	188.1	257.0	270.6	2145

a small size effect and surface effect, and the heating area and heat conduction rate increase, resulting in the apparent activation energy of thermal decomposition decreases. Compared with the raw material, the FOX-7 prepared by microfluidic crystallization has uniform morphology and fewer crystal defects, so it has higher thermal safety.

3.5. Laser Ignition and Combustion Properties. The investigation of ignition and flame propagation characteristics of energetic materials holds significant importance in elucidating their combustion mechanisms and potential applications in propellants. Laser ignition technology, compared to other methods, is relatively mature to study the properties of energetic materials and can be easily applied to the ignition process with solid, liquid, and gas phases.

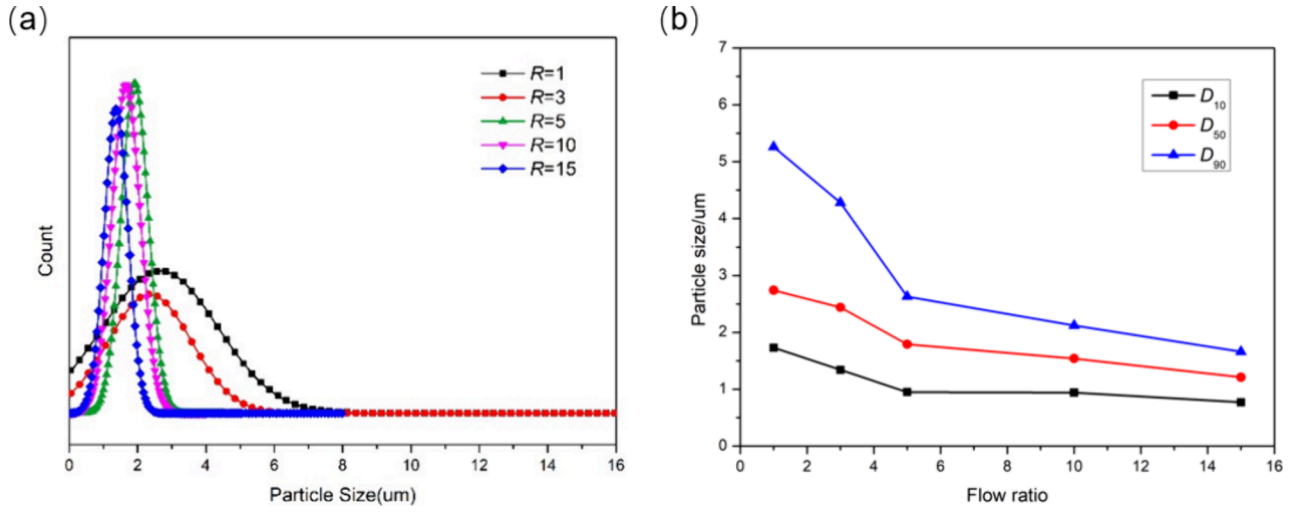

Figure 10. (a) PSDs of FOX-7 samples prepared with different flow ratio R values and (b) influence of flow ratio R on particle size

https://doi.org/10.1021/acsomega.4c10924
ACS Omega 2025, 10, 14042−14051

Table 3. Kinetic Parameters and Thermal Safety Parameters of Ultrafine and Raw FOX-7

samples	T_p (first decomposition process)/°C				E_k/KJ·mol^{-1}	lg(A)/s^{-1}	T_{p0}	T_b
	5 K·min^{-1}	10 K·min^{-1}	15 K·min^{-1}	20 K·min^{-1}				
raw Fox-7	227.7	232.4	235.1	236.2	326.8	32.2	220.6	221.8
ultrafine Fox-7	253.7	257.0	257.2	264.3	257.9	24.6	242.1	243.9

Therefore, the ignition and combustion process of FOX-7 before and after recrystallization by microfluidics were studied by a laser ignition device in this study. The samples were made into ignition specimens, and the laser ignition test was carried out in the power density range of 109.3−299.2W/cm. The ignition delay time curve of the samples, obtained under different laser power densities, is depicted in Figure 12.

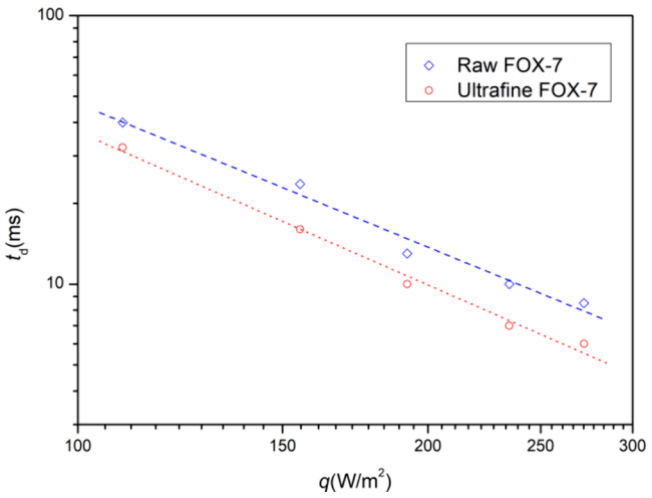

Figure 12. Ignition delay times of ultrafine and raw Fox-7.

The information depicted in Figure 12 indicates that the ignition delay time of both raw materials and ultrafine FOX-7 exhibits a decreasing trend with the increase of the laser power density, while the disparity between the two materials gradually diminishes as the laser power density increases. Notably, under identical power density conditions, the microfluidic-prepared ultrafine FOX-7 demonstrates a significantly shorter ignition delay time compared to the raw material counterpart, indicating lower ignition energy requirements and enhanced ignitability facilitated by the microfluidic method. Figure 13 shows sequential images in the flame propagation process and appearance after ignition of two FOX-7 materials at 169.5W power density. Both of them were successfully ignited and showed self-sustained combustion. Compared with the raw material, the ignition flame of the ultrafine FOX-7 becomes brighter and the flame propagation rate is faster, while the combustion is more complete. This is consistent with the thermal decomposition results, because the small size effect of ultrafine FOX-7 is conducive to increasing the interface contact, and the energy release is more rapid and complete, thus improving the combustion performance of the material.

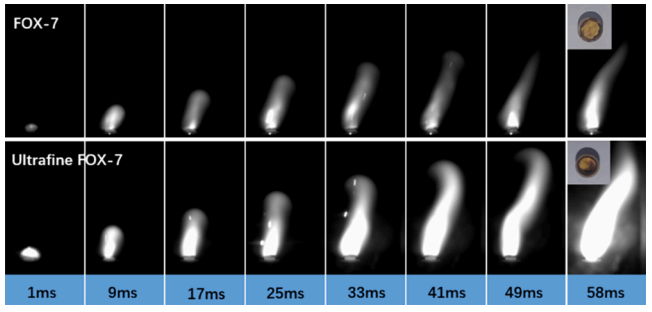

Figure 13. Burning snapshots of ultrafine and raw FOX-7.

4. CONCLUSIONS

A microfluidic crystallization platform was developed for the preparation and crystallization control of ultrafine FOX-7. The prepared ultrafine FOX-7 exhibits a smaller particle size, narrower particle size distribution, reduced crystal defects, and enhanced sphericity compared with the traditional method-prepared materials. By manipulating reaction parameters, such as the solvent/antisolvent system, reagent concentration, and flow ratio within the microfluidic platform, both the morphology and particle size of FOX-7 could be easily controlled. Thermochemical performance tests revealed that microfluidic-prepared ultrafine FOX-7 has better thermal stability, higher energy release efficiency, and more complete combustion compared with the raw material. The microfluidic strategy represents a safe and efficient approach to preparing ultrafine FOX-7 particles with high comprehensive performances.

AUTHOR INFORMATION

Corresponding Author

Xuanjun Wang − *Zhijian Laboratory, Rocket Force University of Engineering, Xi'an 710038, China*; Email: wangxj503@sina.com

Authors

Hanyu Jiang − *Zhijian Laboratory, Rocket Force University of Engineering, Xi'an 710038, China; National Key Laboratory of Energetic Materials, Xi'an Modern Chemistry Research Institute, Xi'an 710065, China*; orcid.org/0000-0001-8823-8870

Siyu Xu − *National Key Laboratory of Energetic Materials, Xi'an Modern Chemistry Research Institute, Xi'an 710065, China*

Jin Yu − *National Key Laboratory of Energetic Materials, Xi'an Modern Chemistry Research Institute, Xi'an 710065, China*

Zihao Zhang − *National Key Laboratory of Energetic Materials, Xi'an Modern Chemistry Research Institute, Xi'an 710065, China*

Xiaogang Mu − *Zhijian Laboratory, Rocket Force University of Engineering, Xi'an 710038, China*

Taizhong Huang − *Shandong Provincial Key Laboratory of Fluorine Chemistry and Chemical Materials, School of Chemistry and Chemical Engineering, University of Jinan, Jinan 250022, China*; orcid.org/0000-0003-0648-5021

Fengqi Zhao − *National Key Laboratory of Energetic Materials, Xi'an Modern Chemistry Research Institute, Xi'an 710065, China*; orcid.org/0000-0003-3400-7131

https://doi.org/10.1021/acsomega.4c10924
ACS Omega 2025, 10, 14042−14051

Complete contact information is available at:
https://pubs.acs.org/10.1021/acsomega.4c10924

Notes

The authors declare no competing financial interest.

■ ACKNOWLEDGMENTS

This research was financially supported by the National Natural Science Foundation of China (no. 52027809).

■ REFERENCES

(1) Latypov, N. V.; Bergman, J.; Langlet, A.; Wellmar, U.; Bemm, U. Synthesis and reactions of 1, 1-diamino-2, 2-dinitroethylene. *Tetrahedron* **1998**, *54*, 11525−11536.
(2) Yuan, B.; Yu, Z.; Bernstein, E. R. Initial decomposition mechanism for the energy release from electronically excited energetic materials: FOX-7 (1, 1-diamino-2, 2-dinitroethene, $C_2H_4N_4O_4$). *J. Chem. Phys.* **2014**, *140*, No. 074708.
(3) Song, L.; Zhao, F. Q.; Xu, S. Y.; Ju, X. H.; Ye, C. C. Crystal Morphology prediction and Anisotropic evolution of 1, 1-Diamino-2, 2-dinitroethylene (FOX-7) by Temperature Tuning. *Sci. Rep.* **2020**, *10*, 2317.
(4) Anniyappan, M.; Talawar, M. B.; Gore, G. M.; Venugopalan, S.; Gandhe, B. R. Synthesis, characterization and thermolysis of 1, 1-diamino-2, 2-dinitroethylene (FOX-7) and its salts. *J. Hazard. Mater.* **2006**, *137*, 812−819.
(5) Šimková, L.; Klíma, J.; Sazama, P.; Ludvík, J. Electrochemical investigation of 2, 2-dinitroethene-1, 1-diamine (FOX-7) in aqueous media. *J. Solid State Electrochem.* **2011**, *15*, 2133−2139.
(6) Trzciński, W. A.; Chyłek, Z. Modelling of the Synthesis of 1, 1-Diamino-2, 2-dinitroethene (DADNE). *Cent. Eur. J. Energy Mater.* **2012**, *9*, 101−117.
(7) Vo, T. T.; Zhang, J.; Parrish, D. A.; Twamley, B.; Shreeve, J. N. M. New roles for 1, 1-diamino-2, 2-dinitroethene (FOX-7): halogenated FOX-7 and azo-bis (diahaloFOX) as energetic materials and oxidizers. *J. Am. Chem. Soc.* **2013**, *135*, 11787−11790.
(8) Latypov, N. V.; Johansson, M.; Holmgren, E.; Sizova, E. V.; Sizov, V. V.; Bellamy, A. J. On the synthesis of 1, 1-diamino-2, 2-dinitroethene (FOX-7) by nitration of 4, 6-dihydroxy-2-methylpyrimidine. *Org. Process Res. Dev.* **2007**, *11*, 56−59.
(9) Chen, K.; Wang, J.; Feng, Y.; Huang, X.; Wang, T.; Wang, N.; Hao, H. Development of continuous tubular crystallizer. *Chem. Ind. Eng.* **2022**, *39*, 36−53.
(10) Schaber, S. D.; Gerogiorgis, D. I.; Ramachandran, R.; Evans, J. M.; Barton, P. I.; Trout, B. L. Economic analysis of integrated continuous and batch pharmaceutical manufacturing: a case study. *Ind. Eng. Chem. Res.* **2011**, *50*, 10083−10092.
(11) Ildefonso, M.; Revalor, E.; Punniam, P.; Salmon, J. B.; Candoni, N.; Veesler, S. Nucleation and polymorphism explored via an easy-to-use microfluidic tool. *J. Cryst. Growth* **2012**, *342*, 9−12.
(12) Edel, J. B.; Fortt, R.; DeMello, J. C.; DeMello, A. J. Microfluidic routes to the controlled production of nanoparticles. *Chem. Commun.* **2002**, 1136−1137.
(13) Mark, D.; Haeberle, S.; Roth, G.; von Stetten, F.; Zengerle, R. Microfluidic lab-on-a-chip platforms: requirements, characteristics and applications. *Chem. Soc. Rev.* **2010**, *39*, 1153−1182.
(14) Manz, A.; Graber, N.; Widmer, H.Á. Miniaturized total chemical analysis systems: a novel concept for chemical sensing. *Sens. Actuators, B* **1990**, *1*, 244−248.
(15) Wang, Q.; Steinbock, O. Materials synthesis and catalysis in microfluidic devices: Prebiotic chemistry in mineral membranes. *ChemCatChem.* **2020**, *1*, 63−74.
(16) Ran, R.; Sun, Q.; Baby, T.; Wibowo, D.; Middelberg, A. P.; Zhao, C. X. Multiphase microfluidic synthesis of micro-and nanostructures for pharmaceutical applications. *Chem. Eng. Sci.* **2017**, *169*, 78−96.
(17) Lagus, T. P.; Edd, J. F. A review of the theory, methods and recent applications of high-throughput single-cell droplet microfluidics. *J. Phys. D: Appl. Phys.* **2013**, *46*, No. 114005.
(18) Ran, R.; Sun, Q.; Baby, T.; Wibowo, D.; Middelberg, A. P.; Zhao, C. X. Multiphase microfluidic synthesis of micro-and nanostructures for pharmaceutical applications. *Chem. Eng. Sci.* **2017**, *169*, 78−96.
(19) Li, Z. Y.; Huang, M.; Wang, X. K.; Zhu, Y.; Li, J. S.; Wong, C. C.; Fang, Q. Nanoliter-scale oil-air-droplet chip-based single cell proteomic analysis. *Anal. Chem.* **2018**, *90*, 5430−5438.
(20) Yu, J.; Xu, S. Y.; Jiang, H. Y.; Zhao, F. Q. Application and development trend of microfluidic technology in preparation of energetic materials. *Chin. J. Explos. Propellants* **2022**, *45*, 439−451.
(21) Lee, J. H. Gas sensors using hierarchical and hollow oxide nanostructures: overview. *Sens. Actuators* **2009**, *B 140*, 319−336.
(22) H. H., Shi Investigations on crystal nucleation and crystal morphology manipulation under microfluidic conditions, Ph.D., Tianjin University, 2020.
(23) Shi, J. Y.; Zhu, P.; Shen, R. Q. Reviews on the structure and morphology control of explosives based on microfluidic technology. *Chin. J. Energy Mater.* **2022**, *30*, 511−526.
(24) Zhao, S.; Wu, J.; Zhu, P.; Xia, H.; Chen, C.; Shen, R. Microfluidic platform for preparation and screening of narrow size-distributed nanoscale explosives and supermixed composite explosives. *Ind. Eng. Chem. Res.* **2018**, *57*, 13191−13204.
(25) Shi, J.; Zhu, P.; Zhao, S.; Xu, C.; Yan, F.; Shen, R.; Xia, H.; Jiang, H.; Xu, S.; Zhao, F. Continuous spheroidization strategy for explosives with micro/nano hierarchical structure by coupling microfluidics and spray drying. *Chem. Eng. J.* **2021**, *412*, No. 128613.
(26) Zhang, X. X.; Xue, Z. H.; Wang, Z.; Yan, Q. L. Thermal Reactivity of High-Density Hybrid Hexahydro-1, 3, 5-trinitro-1, 3, 5-triazine Crystals Prepared by a Microfluidic Crystallization Method. *Langmuir* **2023**, *39*, 7503−7513.
(27) Lee, C. Y.; Chang, C. L.; Wang, Y. N.; Fu, L. M. Microfluidic mixing: A review. *Int. J. Mol. Sci.* **2011**, *12*, 3263−3287.
(28) Lin, Y. Numerical characterization of simple three-dimensional chaotic micromixers. *Chem. Eng. J.* **2015**, *277*, 303−311.
(29) Becker, H.; Locascio, L. E. Polymer microfluidic devices. *Talanta* **2002**, *56*, 267−287.
(30) Gao, Z.; Wu, Y.; Gong, J.; Wang, J.; Rohani, S. Continuous crystallization of α-form L-glutamic acid in an MSMPR-Tubular crystallizer system. *J. Cryst. Growth* **2019**, *507*, 344−351.
(31) Zhao, Q.; Liu, N.; Wang, B.; Wang, W. A study of solvent selectivity on the crystal morphology of FOX-7 via a modified attachment energy model. *RSC Adv.* **2016**, *6*, 59784−59793.
(32) Zhao, X.; Cao, D.; Wang, J.; Chen, L.; Zhang, Y.; Zhou, C. Solubility and Crystallization of FOX-7 in DMSO-H2 O, DMSO-EtOH and DMSO-ACE Binary Mixed Solvents. *Chin. J. Explos. Propellants* **2019**, *42*, 473−479.
(33) Marsh, B. D. Crystal size distribution (CSD) in rocks and the kinetics and dynamics of crystallization: I. Theory, Contr. *Mineral. Petrol.* **1988**, *99*, 277−291.
(34) H., Ren, Q., Jiao *Micro/nano energetic materials*; Beijing Institute of Technology Press, Beijing, 2015.
(35) Evers, J.; Klapötke, T. M.; Mayer, P.; Oehlinger, G.; Welch, J. α- and β-FOX-7, polymorphs of a high energy density material, studied by X-ray single crystal and powder investigations in the temperature range from 200 to 423 K. *Inorg. Chem.* **2006**, *45*, 4996−5007.
(36) Crawford, M. J.; Evers, J.; Göbel, M.; Klapötke, T. M.; Mayer, P.; Oehlinger, G.; Welch, J. M. γ-FOX-7: structure of a high energy density material immediately prior to decomposition. *Propellants Explos. Pyrotech.* **2007**, *32*, 478−495.
(37) Wang, K.; Zhang, W.; Phelan, R.; Morris, M. A.; Holmes, J. D. Direct fabrication of well-aligned free-standing mesoporous carbon nanofiber arrays on silicon substrates. *J. Am. Chem. Soc.* **2007**, *129*, 13388−13389.
(38) Prodan, E. Localization phenomena of topochemical reactions. *J. Therm. Anal. Calorim.* **1984**, *29*, 941−948.

(39) Zohari, N.; Keshavarz, M. H.; Seyedsadjadi, S. A. The advantages and shortcomings of using nano-sized energetic materials. *Cent. Eur. J. Energy Mater.* **2013**, *10*, 135−147.
(40) Kissinger, H. E. Reaction kinetics in differential thermal analysis. *Anal. Chem.* **1957**, *29*, 1702−1706.
(41) Criado, J.; Sánchez-Jiménez, P.; Pérez-Maqueda, L. Critical study of the isoconversional methods of kinetic analysis. *J. Therm. Anal. Calorim.* **2008**, *92*, 199−203.
(42) Tonglai, Z.; Rongzu, H.; Yi, X.; Fuping, L. The estimation of critical temperatures of thermal explosion for energetic materials using non-isothermal DSC. *Thermochim. Acta* **1994**, *244*, 171−176.

https://doi.org/10.1021/acsomega.4c10924
ACS Omega 2025, 10, 14042−14051